Domain wall dynamics in antiferromagnetically coupled double-lattice systems

Eloi Haltz

Université Paris-Saclay, CNRS, Laboratoire de Physique des Solides, 91405 Orsay, France
and School of Physics and Astronomy, University of Leeds, Leeds LS2 9JT, United Kingdom

Sachin Krishnia, Léo Berges, Alexandra Mougin, and João Sampaio *

Université Paris-Saclay, CNRS, Laboratoire de Physique des Solides, 91405 Orsay, France

In ferromagnetic materials, the rich dynamics of magnetic domain walls (DWs) under a magnetic field or current has been successfully described using the well-known q-φ analytical model. We demonstrate here that this simple unidimensional model holds for multiple-sublattice materials such as ferrimagnetic alloys or synthetic antiferromagnets (SAFs) by using effective parameters, and it is in excellent agreement with double-lattice micromagnetic simulations. We obtain analytical laws for the DW velocity and internal precession angle as a function of net magnetization for different driving forces (magnetic field, spin transfer, and spin-orbit torques) and different propagation regimes in ferrimagnetic alloys and SAFs. The model predicts that several distinctive dynamical features occur near or at the magnetic and the angular compensation points when the net magnetization or the net angular momentum of the system vanishes, and we discuss the experimental observations that have been reported for some of them. Using a higher degree-of-freedom analytical model that accounts for inter-sublattice distortions, we give analytical expressions for these distortions that agree with the micromagnetic simulations. This model shows that the DW velocity and precession rate are independent of the strength of the intersublattice exchange coupling, and it justifies the use of the simpler effective parameters model.

I. INTRODUCTION

Antiferromagnetically coupled two-lattice magnetic systems, such as antiferromagnets, ferrimagnets, or synthetic antiferromagnets (SAFs), offer a promising path toward much faster, denser, more robust and efficient spintronic devices [1]. Their decreased net magnetization reduces the vulnerability to external fields and to cross-talk from adjacent devices, allowing for higher storage density and increased robustness. Secondly, the reduced net angular momentum leads to drastically faster magnetic dynamics. Promising theoretical results and experimental observations have been recently obtained in such multilattice magnetic systems [2,3], multilayers architectures [4–6], or synthetic alloys [7–13]. In particular, it has been shown that the antiferromagnetic coupling between sublattices brings the characteristic frequency of magnetization dynamics up to the THz range [14–18].

Antiferromagnets are hard to probe and manipulate experimentally as the two sublattices are of the same nature and thus are perfectly balanced. An interesting alternative are systems that mix two distinct sublattices, allowing for a selectivity in both the reading and the manipulation of the antiferromagnetic order. Two very promising and versatile classes of such systems are studied: in one class the sublattices are spatially merged and consist of two different chemical species [Fig. 1(a)], such as rare earth/transition metal ferrimagnetic alloys (RE-TM), and in the other the two sublattices are spatially separated [Fig. 1(b)], such as in synthetic antiferromagnets (SAFs) where two magnetic films are antiferromagnetically coupled through the Ruderman-Kittel-Kasuya-Yosida (RKKY) interaction [19–21]. In both systems, it is possible to change the balance between the moments of the sublattices by changing the composition or temperature of the ferrimagnetic alloy [22] or the thickness of the layers of the SAF [20]. Two particular configurations are of special interest: the magnetic compensation point (MCP), where the the net magnetization of the system vanishes, and the angular compensation point (ACP), where the net angular momentum vanishes. Depending on the material, these compensation points are distinct if the two sublattices are chemically different [23], or they coincide if they have the same nature.

These systems are already well known for their interesting static properties [21,22]. More recently, the study of dynamics in such systems has produced many interesting results [1]. However, the dynamics of magnetic textures in these systems still lacks a clear, well-understood, and straightforward description. Experimental results are often subject to apparently conflicting interpretations, particularly near the compensation points, where the dynamics differs the most from the well-studied ferromagnetic case.

In this article, the dynamics of double-sublattice films is investigated analytically and numerically through the prism of magnetic domain wall (DW) dynamics. In Sec. II, we discuss

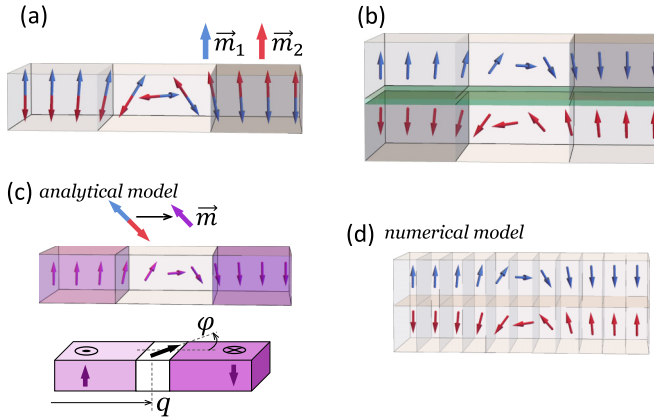* joao.sampaio@universite-paris-saclay.fr

FIG. 1. Illustrations of the two considered systems and the used models. (a) DW in a perpendicularly magnetized double-lattice system where the two lattices are spatially merged, such as in a ferrimagnetic alloy, and (b) in a system with spatially separated sublattices, such as a SAF. (c) Analytical q-φ model, with a single effective ferromagnetic DW with the effective parameters. (d) Numerical, spatially discretized model.

different models for DW dynamics. In Sec. III, we give analytical laws and we evaluate their validity for the DW dynamics under different driving forces: magnetic field, spin transfer torque (STT), and interfacial spin orbit torque (SOT). Finally, we consider the effects of finite coupling in Sec. IV. For the reader's convenience, all used symbols and their definitions are listed in Table V. We have chosen to use the material parameters of two examples of real systems: the RE-TM ferrimagnetic alloy CoGd, and the SAF CoFeB/Ru/CoFeB [Figs. 1(a) and 1(b)]. These two systems illustrate the cases of spatially merged (CoGd) and segregated (SAF) antiferromagnetically coupled sublattices, as well as of systems with distinct (CoGd) and coinciding (SAF) compensation points.

II. MODELING DW DYNAMICS IN MULTILATTICE SYSTEMS

We use three models (two analytical and one numerical) of DW dynamics in double-lattice systems. The first is the well-studied ferromagnetic q-φ analytical model. We expand it to double-lattice systems using effective parameters [24], which defines an equivalent ferromagnetic material in the limit of infinite coupling between the sublattices [Fig. 1(c)]. We will then compare it to the far less restricted numerical micromagnetic double-lattice model [Fig. 1(d)]. In Sec. IV, where we study the effects of finite coupling and deviations from a perfect antialignment of the sublattices, we will use a double q-φ analytical model [Fig. 6(d)].

A. Effective parameters

The dynamics of a magnetization distribution $\mathbf{M}(\mathbf{r}, t) = M_S \mathbf{m}(\mathbf{r}, t)$ is described by the Landau-Lifshitz-Gilbert equation (LLG) [25,26]:

$$\partial_t \mathbf{m} = -\mu_0 \gamma \mathbf{m} \times \mathcal{H} + \alpha \mathbf{m} \times \partial_t \mathbf{m} + (\gamma / M_S) \boldsymbol{\tau}. \quad (1)$$

$\gamma = M_S / L_S$ is the gyromagnetic ratio taken as positive in ferromagnets, M_S is the spontaneous magnetization, L_S is the

angular momentum density, α is the Gilbert damping parameter, and $\mathcal{H} \equiv \frac{-1}{\mu_0 M_S} \delta_{\mathbf{m}} U$ is the effective field associated with $\delta_{\mathbf{m}} U$, the variational derivative of the total energy density $U(\mathbf{m}(\mathbf{r}))$ (defined in Appendix B). $\boldsymbol{\tau}$ accounts for nonconservative torques per unit volume applied on $\mathbf{m}$, such as STT or SOT. When dealing with effective parameters, it is helpful to express the LLG equation in terms of angular momentum density L_S and of the product of the damping parameter α with L_S [27], $L_\alpha \equiv \alpha L_S$, which yields

$$\partial_t \mathbf{m} = \frac{1}{L_S} (\mathbf{m} \times \delta_{\mathbf{m}} U + L_\alpha \mathbf{m} \times \partial_t \mathbf{m} + \boldsymbol{\tau}), \quad (2)$$

which can be rewritten in its explicit form:

$$\partial_t \mathbf{m} = \frac{L_S}{L_S^2 + L_\alpha^2} (\mathbf{m} \times \delta_{\mathbf{m}} U + \boldsymbol{\tau})$$
$$+ \frac{L_\alpha}{L_S^2 + L_\alpha^2} \mathbf{m} \times (\mathbf{m} \times \delta_{\mathbf{m}} U + \boldsymbol{\tau}). \quad (3)$$

This form emphasizes the two components of the dynamics of magnetization. When $\boldsymbol{\tau} = 0$, $\mathbf{m}$ precesses around $\delta_{\mathbf{m}} U$ with a rate $|\delta_{\mathbf{m}} U| L_S / (L_S^2 + L_\alpha^2)$ and relaxes toward $-\delta_{\mathbf{m}} U$ with a rate $|\delta_{\mathbf{m}} U| L_\alpha / (L_S^2 + L_\alpha^2)$. The energy variation due to dissipation is [26,28]

$$d_t U = -L_\alpha |\partial_t \mathbf{m}|^2 = -\frac{L_\alpha}{L_S^2 + L_\alpha^2} |\mathbf{m} \times \delta_{\mathbf{m}} U|^2, \quad (4)$$

which is always negative (thanks to $L_\alpha > 0$) or zero when and only when $\mathbf{m} \parallel \delta_{\mathbf{m}} U$, as is physically expected.

The STT can be written as $\boldsymbol{\tau}_{\text{STT}} = -(L_S \mathbf{u} \cdot \nabla)\mathbf{m} + \mathbf{m} \times (\beta L_S \mathbf{u} \cdot \nabla)\mathbf{m}$ with $L_S \mathbf{u} = PJ\hbar/(2e)\mathbf{e}_J$, and β is the nonadiabatic parameter [29], $J\mathbf{e}_J$ is the current density, and P is the current spin polarization. The SOT is separable in field-like (FL) and dampinglike (DL) terms: $\boldsymbol{\tau}_{\text{SOT}} = \tau_{\text{FL}} \, \mathbf{m} \times \boldsymbol{\sigma} + \tau_{\text{DL}} \, \mathbf{m} \times (\mathbf{m} \times \boldsymbol{\sigma})$, with $\boldsymbol{\sigma}$ the orientation of the spin accumulation. When τ_{DL} is due to SHE, $\boldsymbol{\sigma} = \pm \mathbf{e}_J \times \mathbf{z}$ and $\tau_{\text{DL}} = \tau_{\text{SHE}} = J\theta_{\text{SHE}} \hbar / (2et)$, with t the film thickness and θ_{SHE} the SHE angle [1].

In a material with two magnetic sublattices (indexed "1" and "2"), the direction of the magnetization of each sublattice ($\mathbf{m}_1$ or $\mathbf{m}_2$) can be described by the LLG equation with the respective parameters (with individual spontaneous magnetizations M_1 and M_2, angular momentum densities L_1 and L_2, etc.). The total energy includes an exchange interlattice coupling interaction $U_{12} = -J_{\text{AF}} \mathbf{m}_1 \cdot \mathbf{m}_2$ (with $J_{\text{AF}} < 0$ for antiferromagnetic coupling) [4,5,30–32]. In SAFs, the interlattice coupling is interfacial and provided by RKKY. Additionally, the dipolar interactions may also contribute to the interlattice coupling. If the applied torques are much smaller than the interlattice coupling, the antialignment of magnetic moments $\mathbf{m}_1$ and $\mathbf{m}_2$ should not be significantly disturbed. If we consider the approximation $\mathbf{m}_1 = -\mathbf{m}_2$, the magnetic order in the system can be described by an equivalent effective ferromagnetic film with $\mathbf{m} = \mathbf{m}_1 = -\mathbf{m}_2$, similar to what was done in Refs. [24,31] and illustrated in Fig. 1(c). To find the parameters of the equivalent material, we consider the sum of the two individual LLG equations integrated along the thickness of the film, $(L_1 t_1) \text{LLG}_1(\mathbf{m}) + (L_2 t_2) \text{LLG}_2(-\mathbf{m})$, which allows removing the coupling energy term. Then, the effective parameters can be deduced by comparing this sum to the

effective LLG equation (also integrated along the thickness) $(L_S t)$LLG($\mathbf{m}$) term-by-term, yielding

$$M_S = (M_1 t_1 - M_2 t_2)/t, \quad L_S = (L_1 t_1 - L_2 t_2)/t,$$
$$L_\alpha = (L_{\alpha 1} t_1 + L_{\alpha 2} t_2)/t. \tag{5}$$

From hereon, the parameters of the sublattices are indexed 1 or 2, while the effective parameters of the equivalent ferromagnet are not. As before, the effective γ is M_S/L_S and the effective α is L_α/L_S. If the two sublattices are in spatially separated layers with thicknesses t_1 and t_2, such as in a SAF or in a multilayer ferrimagnet, the effective thickness is $t = t_1 + t_2$, while if the two lattices are spatially merged, such as in a single-layer ferrimagnetic alloy or antiferromagnet, $t = t_1 = t_2$ instead. The MCP is reached when $M_1 t_1 = M_2 t_2$ and the ACP when $L_1 t_1 = L_2 t_2$. If the two sublattices are the same, $\gamma_1 = \gamma_2$ and the two compensation points coincide. Conversely, if the two sublattices are different (i.e., $\gamma_1 \neq \gamma_2$), the two compensation points are distinct [23]. A similar effective parameter approach could be applied to the case of ferromagnetic coupling or for more than two sublattices, with analogous equations.

The effective $\delta_{\mathbf{m}} U$ is determined using the derivation chain rule: $\delta_{\mathbf{m}} U = \delta_{\mathbf{m}_1} U \, \partial_{\mathbf{m}} \mathbf{m}_1 + \delta_{\mathbf{m}_2} U \, \partial_{\mathbf{m}} \mathbf{m}_2 = \delta_{\mathbf{m}_1} U - \delta_{\mathbf{m}_2} U$. The effective micromagnetic energy parameters (such as the exchange stiffness A, the uniaxial anisotropy K, or the DMI D, as defined in Appendix B) can then be deduced:

$$A = (A_1 t_1 + A_2 t_2)/t, \quad K = (K_1 t_1 + K_2 t_2)/t - K_{\text{dipolar}},$$
$$D = (D_1 t_1 + D_2 t_2)/t. \tag{6}$$

All subsequent system parameters, such as the DW width parameter $\Delta = \sqrt{A/K}$, can be calculated for the effective system by using the effective parameters. In the expression of K, we included K_{dipolar}, the approximation of the dipolar-field-induced shape anisotropy valid in films thinner than the considered magnetic textures. The dipolar field is very different in antiferromagnetically coupled systems with spatially merged and separated sublattices. With merged sublattices, $K_{\text{dipolar}} = \frac{\mu_0}{2} M_S^2$ (zero at MCP as the dipolar field vanishes), and with spatially separated sublattices, $K_{\text{dipolar}} = \frac{\mu_0}{2}(M_1^2 t_1 + M_2^2 t_2)/t$ (which is always finite).

Effective parameters can also be found for the current-induced torques:

$$P = (P_1 t_1 - P_2 t_2)/t, \quad u = \frac{\hbar/2}{L_S} \frac{PJ}{e},$$
$$\beta = (\beta_1 P_1 t_1 + \beta_2 P_2 t_2)/(Pt), \quad \tau_{\text{FL}} = (\tau_{\text{FL1}} t_1 - \tau_{\text{FL2}} t_2)/t,$$
$$\tau_{\text{DL}} = (\tau_{\text{DL1}} t_1 + \tau_{\text{DL2}} t_2)/t, \quad \theta_{\text{SHE}} = \theta_{\text{SHE},1} + \theta_{\text{SHE},2},$$
$$\tau_{\text{SHE}} = J\theta_{\text{SHE}}\hbar/(2et). \tag{7}$$

Note that torques that are even in $\mathbf{m}$ add up (e.g., τ_{DL}), while torques that are odd subtract (e.g., τ_{FL}) [30]. The different susceptibilities to spin current (STT or SOT) of the sublattices are accounted for by the different polarization factors P_1 and P_2 and different spin Hall angles $\theta_{\text{SHE},1}$ and $\theta_{\text{SHE},2}$.

While in a ferromagnet almost all these quantities were constant and positive, the effective parameters, with the

exception of L_α, are signed and some may become zero or diverge ($\pm\infty$) at the compensation points (when $M_S \to 0$ or $L_S \to 0$) or when $P \to 0$. All effective fields diverge at MCP (such as, e.g., $H_{\text{DMI}} = \frac{D/\Delta}{\mu_0 M_S}$; see Fig. 2), and the parameters γ and α diverge and change sign at ACP. β diverges at $P \to 0$. However, none of these divergences leads to nonphysical behaviors (like, e.g., an infinite $\partial_t \mathbf{m}$) as all the terms of the LLG written in the form of Eq. (3) [$\delta_{\mathbf{m}} U$, $L_S/(L_S^2 + L_\alpha^2)$, τ_{SOT}, $L_S u$, $L_S \beta u$, …] remain noninfinite even at the compensation points. Likewise, even if α diverges at ACP, L_α remains finite and positive, which ensures that the dissipation rate [Eq. (4)] is always negative. In Ref. [33], a new definition of α was given to avoid divergence at ACP. However, this is not necessary as the dissipation rate [Eq. (4)] is not given by α, which does diverge, but by $L_\alpha = \alpha M_S/\gamma$, which does not [26,34].

Many effective parameters can be experimentally measured with usual techniques (e.g., M_S and K with magnetometry, current-induced torques by second-harmonic Hall voltage [35], etc.), while sublattice parameters have to be selectively probed (e.g., x-ray dichroism in ferrimagnetic alloys).

B. Collective coordinates model in the limit of strong coupling

A very useful model of DW dynamics in perpendicularly magnetized ferromagnetic systems is the one-dimensional (1D) q-φ equation [36–38] [Eq. (A1), detailed in Appendix A]. It describes the DW dynamics with two variables (the "collective coordinates"): the DW position q and its in-plane magnetization angle φ (see Fig. 1). Two steady-state DW propagation regimes are predicted [36]: the translational regime at low drive, with a constant velocity and constant DW angle ($v = \dot{q} = \text{const}$ and $\dot{\varphi} = 0$), and the precessional regime at high drive, with an oscillating velocity and precessing DW angle. The two regimes are separated by the Walker threshold [36–39] (indicated by a subscript W) that is determined by DMI and by the in-plane DW anisotropy created by the demagnetization effect (K_{BN}). Note that for a DW driven by SHE alone, the precessional regime does not occur [38]. The q-φ equation can be solved analytically, and it yields simple analytical laws for the translational regime and for the high-drive limit of the precessional regime ("asymptotic precessional regime"). We will also integrate it numerically for the full range of drive. The analytical expressions for the velocity v, the internal angle φ, and the precession rate $\dot{\varphi}$ of a DW driven by field, SOT, or STT in both regimes are shown for reference in Table IV. Note that this 1D model does not account for 2D effects, such as tilting DWs or Bloch lines, that can, in some cases, alter significantly the dynamics of wide DWs.

By applying the effective parameters described before to this model, it is possible to describe the DW dynamics in a multisublattice film, including across the compensation points. The resulting expressions for the DW dynamical parameters are shown in Table I and are expressed with nondiverging parameters, wherever possible. Although some terms in Eq. (A1) diverge at the compensation points, no unphysical behaviors are predicted by this model (e.g., infinite velocity), and all measurable quantities are finite.
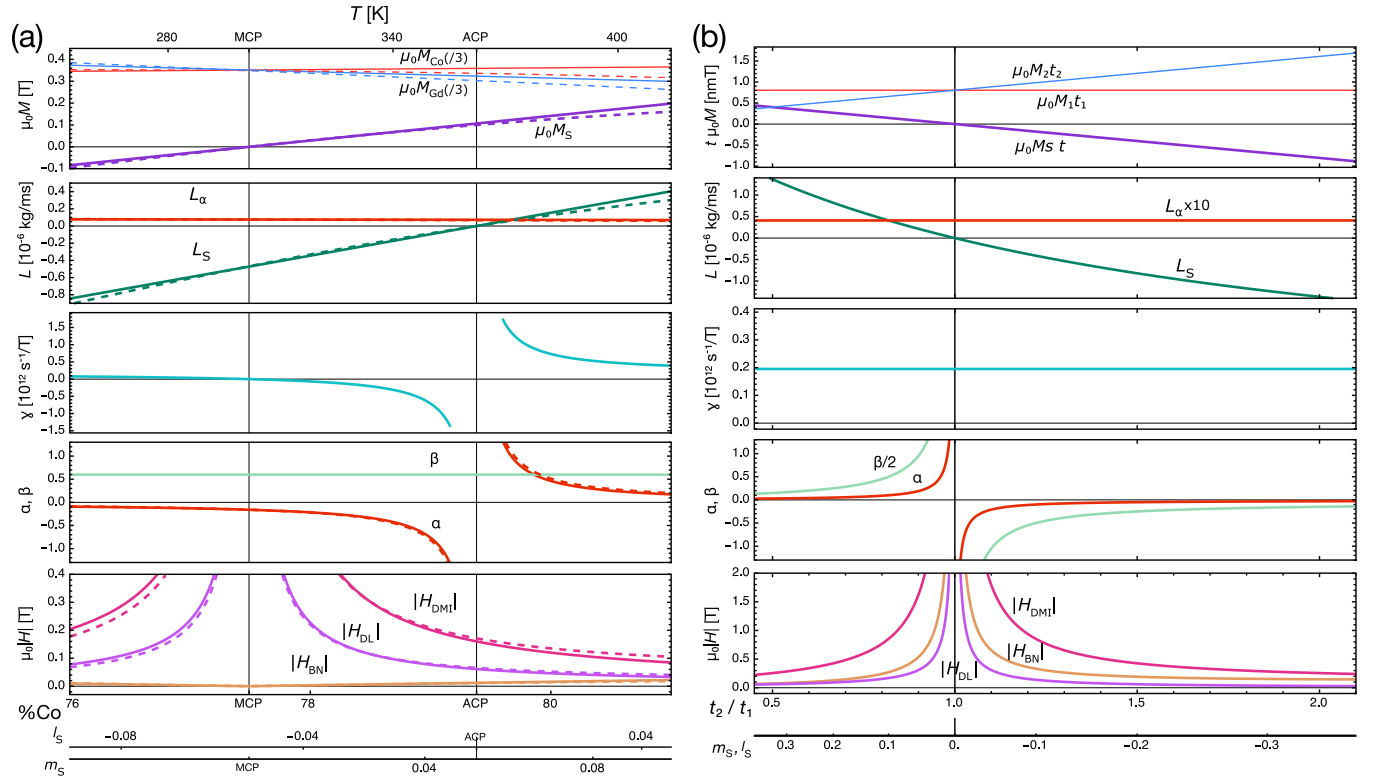
FIG. 2. (a) Effective parameters of the CoGd ferrimagnetic alloy vs temperature and composition (solid and dashed lines, respectively), based on a mean-field model: M_S (and sublattice magnetization), L_S, L_α, γ, α, β, and the effective fields $|H_{BN}|$, $|H_{DMI}|$, and $|H_{DL}| = |\tau_{DL}/(\mu_0 M_S)|$ (at $J = 30$ GA/m^2). (b) Effective parameters for the SAF system vs layer thickness ratio. l_S and m_S are shown in the horizontal bars on the bottom.

C. Numerical modeling of multilattice DW dynamics

There may be deviations from the perfect antialignment of the two sublattices that is assumed in the model above. There could also be other distortions from the assumed 1D DW profile. To verify the validity of the analytical model, we have considered a numerical micromagnetic model by solving the LLG equations using the MUMAX3 software [40]. In Sec. IV we will also address analytically the sublattice misalignment.

To simulate a ferrimagnetic film, we use a sliding simulation mesh with two layers ($128 \times 16 \times 2$ of $2 \times 2 \times 3.8$ nm^3 cells), where the parameters of each layer correspond to the different sublattices of the film. An exchange coupling between mesh layers accounts for the antiferromagnetic inter-sublattice coupling. We have not included the demagnetizing field in the simulations of the CoGd, which is an acceptable approximation in the case of homogeneous and low

TABLE I. q-φ model solutions (from Table IV) with effective parameters for v, φ, $\dot{\varphi}$, and the Walker threshold of a DW driven by field, STT, or SOT, in translational and asymptotic precessional regimes. The Walker thresholds have divergence points (discussed in the text), as do β (at $P = 0$) and u (at $L_S = 0$). However, $L_S u$, $\beta L_S u$, and βP do not diverge. All other shown parameters do not diverge. The top and bottom expressions for φ and Walker thresholds refer to the case of dominant dipolar-induced Bloch-Néel anisotropy (K_{BN}) or dominant DMI (D). Here, $H_x = H_y = \tau_{FL} = 0$.

Field-driven

Translational regime		Walker threshold	Asympt. precessional regime	
$v = \frac{\Delta}{L_\alpha} \mu_0 M_S H$	$\varphi = \begin{cases} \frac{1}{2}\arcsin{(H/H_W)} \\ \arcsin{(H/H_W)} \end{cases}$	$\|H_W\| = \begin{cases} \left\| \frac{L_\alpha}{L_S} \frac{1}{\mu_0 M_S} K_{BN} \right\| \\ \left\| \frac{L_\alpha}{L_S} \frac{1}{\Delta \mu_0 M_S} \frac{\pi}{2} D \right\| \end{cases}$	$v = \frac{\Delta L_\alpha}{L_S^2 + L_\alpha^2} \mu_0 M_S H$	$\dot{\varphi} = \frac{L_S}{L_S^2 + L_\alpha^2} \mu_0 M_S H$

STT-driven

Translational regime		Walker threshold	Asympt. precessional regime	
$v = \frac{\beta}{L_\alpha} L_S u$	$\varphi = \begin{cases} \frac{1}{2}\arcsin(J/J_W) \\ \arcsin(J/J_W) \end{cases}$	$\|J_W\| = \begin{cases} \left\| \frac{L_\alpha}{L_S \beta P - L_\alpha P} \frac{e\Delta}{\hbar/2} K_{BN} \right\| \\ \left\| \frac{L_\alpha}{L_S \beta P - L_\alpha P} \frac{e}{\hbar/2} \frac{\pi}{2} D \right\| \end{cases}$	$v = \frac{L_S + L_\alpha \beta}{L_S^2 + L_\alpha^2} L_S u$	$\dot{\varphi} = \frac{1}{\Delta} \frac{L_S \beta - L_\alpha}{L_S^2 + L_\alpha^2} L_S u$

SOT-driven

Translational regime		
$v = \frac{\Delta}{L_\alpha} \frac{\pi}{2} \tau_{SHE} \cos \varphi$	$\varphi = \arctan{(\tau_{SHE}/\frac{L_\alpha D}{L_S \Delta})}$	

TABLE II. Parameters used in the micromagnetic simulations and models, for the CoGd alloy (determined by the mean-field model for CoGd [41]) and CoFeB/Ru/CoFeB SAF. Intervals (in brackets) refer to the range of variable quantities. The RKKY coupling in the SAF is interfacial ($J_{AF} \sim 1/t$), and so it is written as $J_{RKKY} \equiv J_{AF}t$. P and θ_{SHE} were taken as 1 for convenience.

	CoGd		SAF	
	Co	**Gd**	**"1"**	**"2"**
M_s (MA/m)	[0.82, 0.88]	[0.89, 0.70]	0.8	0.8
t (nm)	3.8	3.8	0.8	[0.6, 1.6]
L_s (10^{-6} kg/ms)	[4.2, 4.5]	[4.0, 5.1]	4.1	4.1
Landé g	2.22	2.0	2.22	2.22
α	0.013	0.02	0.01	0.01
J_{AF}, J_{RKKY}	−264 MJ/m^3		−2 mJ/m^2	
A (pJ/m)	16	0	16	16
K (kJ/m^3)	300	0	450	450
D (mJ/m^2)	0.1	0	0.8	0
P	1	0	1	1
β	0.6	0	0.1	0.1
θ_{SHE}	1	0	1	0
Δ (nm)	[7.3, 7.7]		6	
L_α (nJ s/m^3)	[67, 80]		41	

magnetization systems with a significant DMI [38]. The SAF was simulated in a similar way, but taking into account the demagnetizing field, which is more important in this system, as well as the spatial gap between the layers. Due to the constraints of the spatial discretization method, the simulations of the SAF were done for fewer values of m_S than those of the CoGd.

III. DW DYNAMICS

We examine now the DW dynamics under different driving forces (field, STT, or SOT) using the models described above, in the two example systems: the ferrimagnetic alloy CoGd and a SAF CoFeB/Ru/CoFeB. We compare the analytical laws from the model (Table I, shown as lines in the plots) with the results of the numerical simulations (shown as points). To facilitate the comparison between these two systems and other multisublattice systems, the plots will be expressed in terms of the normalized magnetization and normalized angular momentum density,

$$m_S \equiv (M_S t)/(|M_1 t_1| + |M_2 t_2|),$$
$$l_S \equiv (L_S t)/(|L_1 t_1| + |L_2 t_2|). \qquad (8)$$

The SAF will also be compared to a single-layer system composed of only its layer 1 (i.e., $t_2 = 0$ and $m_S = l_S = 1$).

A. Material parameters

Table II shows the parameters used for these two systems. The chosen parameters are close to experimentally reported values when these were available [4,22,35]; some were chosen for the convenience of presenting the DW dynamics (e.g., $P = \theta_{SHE} = 1$ and constant K). For CoGd, the variations with temperature and with alloy composition of the sublattice magnetizations, M_{Co} and M_{Gd}, were calculated using mean field

theory, and the respective angular momenta were calculated using the Landé g factors in the table (see Refs. [22,41] for details). Figure 2(a) shows the variation of magnetization and some effective parameters of the CoGd film versus alloy composition at a fixed temperature (300 K) (full lines and bottom axis) or versus temperature at fixed composition (%Co = 75%) (dotted curves and top axis). The variations with temperature and with composition superpose well, which means that the same set of parameters can be obtained equally by changing the composition or the temperature, in the considered ranges. The two compensation points, MCP and ACP, are clearly visible. Since the two sublattices are of a different nature ($\gamma_1 \neq \gamma_2$), the two compensation points are distinct. γ changes sign twice (crossing zero at the MCP and diverging at the ACP) and α once (diverging at ACP). In the CoGd film, we consider current-induced torques only in the Co sublattice ($P_{Gd} = \theta_{SHE,Gd} = 0$), which is a common assumption in RE-TM alloys where mostly the TM sublattice is active in the spin transport [12].

To tune the sublattices in the SAF, we considered a layer "1" with a fixed thickness ($t_1 = 0.8$ nm) and layer "2" with variable thickness. Figure 2(b) shows the variation of the effective parameters of the SAF versus the layer thickness ratio t_2/t_1. In contrast with CoGd, the two sublattices are of the same material (with $\gamma_1 = \gamma_2$) and so the two compensation points coincide (at $t_2/t_1 = 1$). α diverges and changes sign at the compensation point, but γ is always nonzero and finite. For this system, the DMI and the SHE torque are assumed to be present only in layer "1," which corresponds to a SAF structure with a single heavy metal adjacent layer. The STT is applied in the two layers with the same magnitude ($P_1 = P_2$ and $\beta_1 = \beta_2$).

B. DW driven by field

Figures 3(a1) and 3(a2) and Figs. 3(b1) and 3(b2) show the DW velocity v and precession rate $\dot{\varphi}$ versus the perpendicular field H in CoGd and in the SAF, for different values of l_S. The numerical integration of the q-φ equation [Eq. (A1), lines] matches very well the numerical simulations (points). Fast DW velocities are obtained (a few km/s), which vary in magnitude and direction with m_S, similar to what is reported in experiments [7]. The translational ($\dot{\varphi} = 0$) and precessional ($\dot{\varphi} \neq 0$) regimes are clearly visible, but they do not occur for every l_S (e.g., for $m_S = 0$ or $l_S = 0$).

The dynamics of the DW versus l_S is more clearly seen in Figs. 3(c1) and 3(c2) and in Figs. 3(d1) and 3(d2) where we show the mobility ($v/\mu_0 H$) and the normalized precession rate ($\dot{\varphi}/\mu_0 H$) versus l_S for CoGd and for the SAF. Except for close to ACP, the simulated DW (points) follows the analytical law for the translational regime (green line) at low fields and approaches at large fields the law of the asymptotically precessional regime (red line). In general, the SAF shows significantly higher mobility than CoGd, as the mobility is inversely proportional to L_α (Table I), which is much lower in the SAF (Fig. 2). For both CoGd and SAF, the mobility is reversed and crosses zero at MCP. Physically, this can be understood since the effect of a (moderate) external field is reversed when the sublattice with the largest magnetization changes (i.e., M_S is reversed) and produces no effect if the
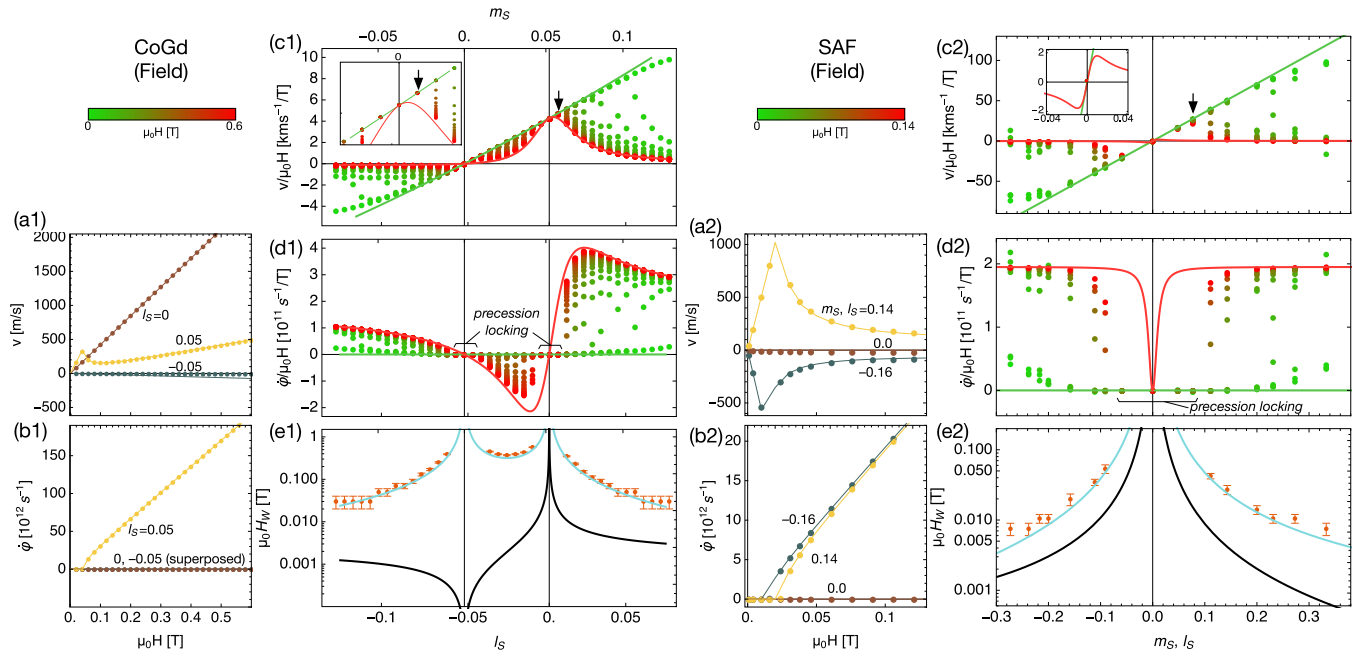
FIG. 3. Field-driven DW dynamics in CoGd (a1)–(e1) and in the SAF (a2)–(e2). (a1),(a2) Velocity v and (b1),(b2) precession rate $\dot{\varphi}$ vs H for a few values of l_S. Points correspond to simulations and lines to the q-φ model [Eq. (A1)]. (c1),(c2) Mobility $v/\mu_0 H$ and (d1),(d2) normalized precession rate $\dot{\varphi}/\mu_0 H$ vs l_S. The points correspond to micromagnetic simulations (low fields in green and high fields in red; see the color scale), and the lines correspond to the translational (green) and asymptotically precessional (red) regimes of the model (Table I). The insets in (c1) and (c2) show the region close to $l_S = 0$. The arrows indicate the point of maximum mobility at the highest field. (e1),(e2) Walker field H_W vs l_S. Points are extracted from (d1) and (d2) and the lines correspond to the model for DMI dominated (blue) and dipolar-field dominated (black) cases.

sublattices are compensated ($M_S = 0$). In the q-φ model (Table I), this is reflected in both regimes as $v \propto M_S H$. The mobility of the precessional regime is comparable to that of the translational regime in CoGd, while in the SAF it is much smaller. The ratio of precessional to translational mobility is given by $(1 + L_S^2/L_\alpha^2)^{-1}$ (Table I), which is indeed much smaller in the SAF than in the CoGd [compare Figs. 2(a) and 2(b)].

The q-φ model also predicts that the DW mobility in the translational regime is not directly dependent on L_S, and so it is not affected by the ACP. In contrast, the mobility in the precessional regime is maximum at ACP as $v/H \propto M_S(L_S^2 + L_\alpha^2)^{-1}$. In the SAF, as the ACP and MCP coincide, the precessional regime mobility shows two maxima (of opposite sign) on either side of the compensation point, and it is zero at that point [see the inset of Fig. 3(c2)].

In CoGd, $\dot{\varphi}$ crosses zero twice at MCP and ACP. In particular, at the ACP the DW propagates without any precession ($\dot{\varphi} = 0$). The q-φ model predicts that indeed $\dot{\varphi} \propto L_S M_S H$, crossing zero at MCP and ACP and reversing its direction between these two points. This is closely related to the magnetic precession rate under field given by the LLG equation [Eq. (3)], which is $\propto \delta_{\mathbf{m}} U L_S = \mu_0 H M_S L_S$. For the SAF, as the two compensation points are superimposed, there is no intermediate region of reversed precession, and $\dot{\varphi}$ is zero at compensation when both $L_S = 0$ and $M_S = 0$. At the point of no precession, the velocities of the translational and precessional regimes predicted by q-φ coincide [see Eq. (A1)].

In the simulations, the precession rate is zero in the vicinity of the compensation point for all tested fields [see Figs. 3(d1)

and 3(d2) and the inset of Fig. 3(c1)]. We call this case precession locking. This phenomenon occurs generally around every point of no precession, and can be understood by analyzing the Walker field H_W, shown in Figs. 3(e1) and 3(e2) for the CoGd and SAF, respectively. The q-φ model solutions are shown with DMI (blue line) and with K_{BN} and no DMI (black line; calculated as described in Appendix A). We note that the SAF shows much higher H_W than the single-layer film of the same material (0.85 mT). The H_W from the simulations follow the DMI solution, as expected, and diverge at ACP and MCP. In the vicinity of the H_W divergence, the DW will propagate in the translational regime even for the highest applied field—leading to precession locking. The model predicts indeed that for the case of dominant DMI, $H_W \propto DL_S^{-1}M_S^{-1}$. Without DMI, $H_W \propto K_{BN}L_S^{-1}M_S^{-1}$. For homogeneous ferrimagnets like CoGd, $K_{BN} \propto M_S^2$, and so H_W diverges at ACP but not at MCP (and is quite small far from ACP). For separated systems like the SAF, K_{BN} remains finite at the compensation, and thus H_W diverges with or without DMI.

An interesting consequence of precession locking is that the maximum mobility at a given applied field does not occur exactly at ACP. If the DW dynamics versus temperature is measured in CoGd at a constant high field, two points of discontinuity will be observed close to ACP corresponding to $H = H_W$. At these points, the DW switches between propagation regimes and its velocity and precession rate change abruptly. This transition can be seen in Fig. 3(c1) where the points at highest field (in red) follow the precessional curve (in red) but switch to the translational curve (in green) near ACP. As a result, the maximum of mobility at high field is
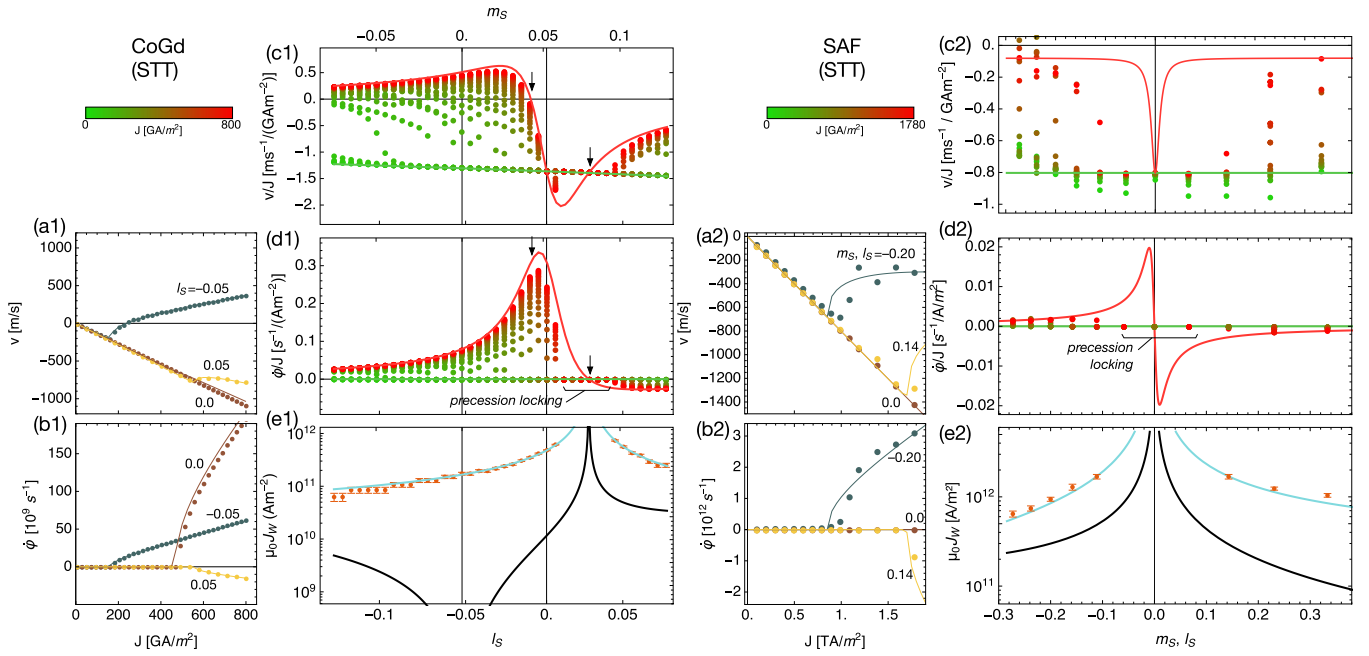
FIG. 4. STT-driven DW dynamics in CoGd (a1)–(e1) and in the SAF (a2)–(e2). (a1),(a2) Velocity v and (b1),(b2) precession rate $\dot{\varphi}$ vs J for a few values of l_S. Points correspond to numerical simulations and lines to the q-φ model [Eq. (A1)]. (c1),(c2) Mobility v/J and (d1),(d2) normalized precession rate $\dot{\varphi}/J$ vs l_S. The dots correspond to micromagnetic simulations (low currents in green and high currents in red; see the color scale). Lines correspond to the translational (green) and asymptotically precessional (red) regimes of the model (Table I). The arrows indicate the point of zero mobility and zero precession, discussed in the main text. (e1),(e2) Walker current J_W vs l_S. Dots are extracted from (d1) and (d2) and the lines correspond to the q-φ model for DMI dominated (blue) and dipolar-field dominated (black) regimes.

not exactly at ACP [see the arrows in Fig. 3(c1)]. As the mobilities of the two propagation regimes converge at ACP, these discontinuities may go unnoticed experimentally, but they may induce errors in the determination of the ACP from the DW mobility peak [13]. The same phenomenon should be observable in a SAF by measuring velocity versus layer thickness (for example, by using a wedge layer).

The mobility peak near ACP was already experimentally observed in a ferrimagnetic alloy (GdFeCo) by Kim *et al.* [7]. The authors observed that the DW mobility increased as the system was heated to a temperature above MCP, up to ∼20 km s^{-1}/T at ∼90 K above MCP, and then decreased quickly after. The authors identified the maximum with ACP by assuming that the DW was in the precessional regime at the peak, although these models predict that it was in the translational regime, and that the maximum is located slightly above ACP.

C. DW driven by STT

Under STT, two nonconservative torques act on the DW, inducing a more complex behavior than with field. We consider that the current interacts only with the Co sublattice of CoGd, whereas it interacts with both layers of the SAF (see Table II). Figures 4(a1) and 4(a2) and Figs. 4(b1) and 4(b2) show the DW velocity v and precession rate $\dot{\varphi}$ versus J for CoGd and the SAF with different values of l_S. The agreement between simulations (points) and the integrated q-φ model (lines) is very good. As in ferromagnets and in the field-driven case, two propagation regimes are visible: the translational regime

at low current ($\dot{\varphi} = 0$) and the precessional regime at high current ($\dot{\varphi} \neq 0$). Interestingly, in the precessional regime in CoGd, the propagation and precession directions change with l_S and with J.

The variation with l_S is more visible in Figs. 4(c1) and 4(c2) and Figs. 4(d1) and 4(d2), which show the mobility (v/J) and the normalized precession rate ($\dot{\varphi}/J$) versus l_S and m_S. For low current (green points), the simulated DW follows the translational laws (green lines), and for higher current (red points), the DW approaches the laws for the asymptotic precessional regime (red lines). In CoGd (for which MCP≠ACP), there are no remarkable variations of these two quantities near MCP, showing that the STT does not depend directly on M_S.

In both systems, the mobility of the translational regime does not vary significantly with l_S when compared with the precessional regime. Indeed, according to the model, the DW mobility in the translational regime is $\beta L_S u / L_\alpha$ (Table I), which is almost constant in the investigated range of parameters [as $\beta L_S u$ is almost constant, Eq. (7)]. Note that the mobility does not depend on M_S. Indeed, although the STT velocity in ferromagnets could be thought to be $\propto u \propto 1/M_S$ (Table IV), once it is explicitly written with nondiverging effective parameters (Table I) no direct dependence on M_S exists.

In the precessional regime, the DW behavior is more complex. In CoGd, there are two remarkable points [marked with arrows in Figs. 4(d1) and 4(c1)]. Slightly before ACP, the propagation direction reverses and the precession rate exhibits a peak. Slightly after ACP, the precession rate changes its sign.
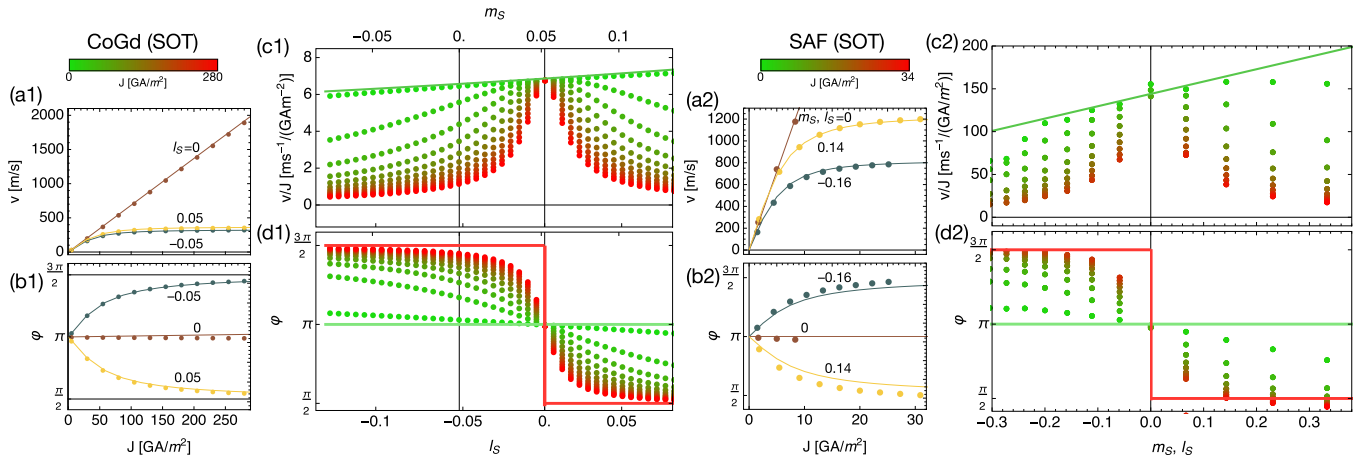
FIG. 5. SHE-driven DW dynamics in CoGd (a1)–(d1) and in the SAF (a2)–(d2). (a1),(a2) Velocity v and (b1),(b2) in-plane magnetization angle φ vs J for different values of l_S. Points correspond to numerical simulations and lines to the q-φ model [Eq. (A1)]. (c1),(c2) Mobility v/J and (d1),(d2) in-plane angle φ vs l_S. The dots correspond to micromagnetic simulations (low currents in green and high currents in red; see the color scale), lines correspond to the asymptotes of the q-φ model (Table I) at low (green) and high current (red). At high current, the model predicts that the velocity is asymptotically limited and the mobility tends to zero, except at ACP.

In the SAF, no propagation reversal occurs, but the mobility is maximum near ACP.

The q-φ model predicts that the reversal of v ($v = 0$) in the precessional regime occurs at $L_S P = -\beta L_\alpha P$. For CoGd, $\beta = \beta_1 > 0$, so the reversal occurs just before ACP. For the SAF, in the studied range, this condition is never satisfied and no reversal occurs [42].

The precession-free point ($\dot{\varphi} = 0$) is predicted at $L_S \beta P = L_\alpha P$. In CoGd, it does not occur at ACP but above, at $L_S = L_\alpha / \beta$ [equivalently, $\beta = \alpha$, visible in Fig. 2(a)]. For the SAF it occurs at compensation (where $L_S = P = 0$), although for a SAF with different materials this point would occur elsewhere as $P \neq 0$ at compensation.

As with field-driven DWs, in the simulations the precession is locked (zero) in the vicinity of the no-precession point predicted by the q-φ model. This can be understood by examining the Walker threshold current J_W, shown in Figs. 4(c1) and 4(c2) for CoGd and the SAF. The J_W extracted from the simulations (points) follows closely the prediction for the DMI dominant case (blue line). The SAF shows a much higher J_W than a single layer of the same material (4×10^{11} A/m^2). With DMI, $J_W > 0$ everywhere. Without DMI (black line), the J_W is proportional to K_{BN}, which is zero at MCP for systems with spatially merged sublattices (CoGd) but is always finite in SAFs. For both cases, the q-φ model predicts that the Walker threshold J_W diverges when $L_S \beta P = L_\alpha P$, which corresponds to the previously discussed precession-free point. For a given maximum J, in the vicinity of this point the Walker current cannot be reached and the DW is precession-locked in the translational regime.

Some of these aspects of the STT-driven DW dynamics have recently been observed by Okuno *et al.* [43] in ferrimagnetic GdFeCo. The authors measured the DW velocity driven simultaneously by field and current for various temperatures. By assuming a linearity between field and current, the authors separated the mean velocity due to the field and the difference of velocities due to the STT. They observed a peak of the STT-induced velocity versus temperature that they attributed

to the ACP (with a limited validity, as discussed above) and a reversal of the STT-induced velocity close to this temperature.

D. DW driven by SHE

We describe here the DW driven by SHE-induced SOT, although the results also apply to any other sources of dampinglike torque of the same form. We do not consider other current-induced torques like the τ_{FL}, which are typically much smaller and lead to more complex dynamics (similar to the STT-driven case). As discussed previously (Table II), the SOT is present only in the Co sublattice of CoGd and in the layer "1" of the SAF.

Figures 5(a1) and 5(a2) and Figs. 5(b1) and 5(b2) show the DW velocity v and the DW in-plane angle φ versus current density J for CoGd and SAF, with different values of l_S. The numerical integrations of the q-φ equation (lines) show an excellent agreement with the micromagnetic simulations (points). As in ferromagnets, the SOT-driven DW only shows a translational regime ($\dot{\varphi} = 0$). φ, initially ≈ 0 at low current, approaches $\pm \pi/2$ with increasing current [as predicted by the model: $\varphi = \arctan(\tau_{SHE} \frac{\Delta L_S}{D L_\alpha})$]. As $v \propto \cos \varphi$, the velocity saturates at high current ($v \to \frac{\pi}{2} D / L_S$). While the propagation direction is always the same, the saturation velocity and φ strongly vary with l_S. In particular, at ACP, the behavior is remarkably different from the ferromagnetic case: the DW propagates without magnetization tilt (φ remains 0) and no saturation is visible.

Figures 5(c1) and 5(c2) and Figs. 5(d1) and 5(d2) show the plots of mobility (v/J) and φ versus l_S. The lines are the limits at low (green) and high (red) current given by the model, and the points correspond to the simulations (green for low current, red for high current). For the CoGd, no remarkable features appear near MCP, showing that the SHE drive, as the STT, does not depend directly on M_S. This contrasts with the effective field created by the DL torque (H_{DL}, shown in Fig. 2), which diverges at MCP, showing that the effective field is not a convenient parameter to characterize the effects

of SOTs in these systems. At low current, φ remains ≈ 0 for all values of m_S and the mobility is large and almost constant (as predicted, $v/\tau_{SHE} \approx \frac{\pi}{2} \Delta/L_\alpha$). At higher current, both quantities vary strongly with m_S. In particular, at ACP, $\varphi = 0$ and changes sign while the mobility shows a peak independent of J. The model indeed predicts that the velocity does not saturate at ACP (the saturation velocity, $\frac{\pi}{2} D/L_S$, diverges), which implies a mobility peak for all currents. For the SAF, this means that the DW can be driven much faster than in the single-layer case (i.e., $t_2 = 0$, which presents a saturation velocity of 306 m/s).

Several experimental reports have shown some of these effects. The variation of the SOT-driven DW velocity with the thickness ratio of a SAF was observed by Yang et al. [4]. The authors measured the DW dynamics in perpendicular-magnetized SAFs with a single Pt adjacent layer, and various layers thicknesses. Both the observed DW mobility and the maximum velocity were greatest at compensation, when the two constituting layers of the SAF were balanced.

Recently, several experimental reports have studied SOT-driven DW dynamics in ferrimagnetic systems. Siddiqui et al. [8] measured the SHE-driven DW velocity in Pt/CoTb/SiN tracks with variable composition observing, for the first time, a mobility peak (versus composition) that could be associated with the ACP. However, the investigated velocity range and the threshold current (required to depin the DW) make it difficult to unambiguously attribute this mobility peak to the ACP. Also, different compositions were measured in different structures, which can present deviations of parameters such as the anisotropy or the DW pinning field.

Caretta et al. [9] studied the SHE-driven DW in Pt/CoGd/TaOx tracks with varying temperature. These experimental results are in very good agreement with the presented model. At high current, a velocity peak versus temperature was observed, which was attributed to the ACP. At low current, however, the peak fades and the velocity did not depend significantly on the temperature.

In our recent work, we studied the SHE-driven DWs in CoFeGd/Pt with variable temperature [13]. A transverse bias field was applied and, using an extension of the described q-φ model to include bias fields, the φ could be determined. A mobility peak (versus temperature) was observed, at which φ vanished and changed sign, showing the precession-free dynamics of the DW at ACP.

Similar conclusions on the velocity versus l_S in ferrimagnets were recently obtained from a theoretical point of view using micromagnetic models and an extended 1D model in [44].

IV. EFFECTS OF FINITE COUPLING

It is important to investigate how the results presented in the previous sections are modified by a finite angle between the sublattice magnetizations ($\mathbf{m}_1 \neq -\mathbf{m}_2$). The strength of the interlattice coupling in ferrimagnetic alloys varies significantly for different alloy compositions or deposition techniques [45–47], and whether the RE-TM is an alloy or is spatially segregated in multilayers. In SAFs, the coupling strength is much weaker than in RE-TM alloys, and it can be
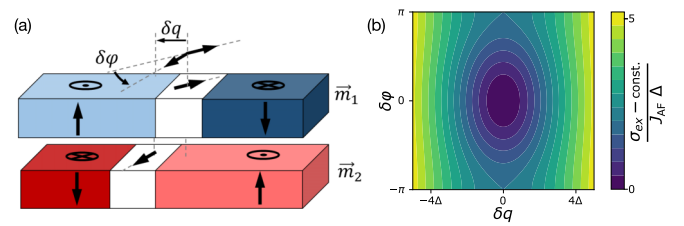

FIG. 6. (a) Diagram of δq and $\delta \varphi$. (b) Surface energy plot of σ_{ex} vs δq and $\delta \varphi$.

modulated (even made ferromagnetic) by altering the spacer layer [20].

A. Collective coordinates model for finite coupling

To study the effects of finite coupling, we developed a collective coordinates model with two coupled sublattices. We consider a DW in a double-lattice system as two rigid ferromagnetic DWs, one for each sublattice, coupled to each other [4,32] [Fig. 6(a)]. The choice of this ansatz for the DW profile is motivated by the fact that it is exact in the two limiting cases of infinite and null interlattice coupling. We consider an ↑↓ DW in the sublattice 1, and a ↓↑ DW in the sublattice 2, with coordinates (q_1, φ_1) and (q_2, φ_2), respectively. The sublattice 1 is arbitrarily chosen as the main one, and we define four more convenient coordinates $q, \delta q, \varphi$, and $\delta \varphi$ [shown in Fig. 6(a)], such as

$$q_1 = q, \quad \varphi_1 = \varphi, \quad q_2 = q + \delta q, \quad \varphi_2 = \varphi + \pi + \delta \varphi.$$

This model allows for some interlattice tilt in the form of lag between the positions of the DWs (δq) or an angle difference between their central antiparallel magnetizations ($\delta \varphi$). A similar model was considered in Refs. [4,44], although without the δq degree of freedom.

The time evolution of the four collective coordinates q, φ, δq, and $\delta \varphi$ is described by using two coupled q-φ equations with different parameters for each sublattice, with an additional energy term, σ_{ex}, that accounts for the interlattice coupling energy per unit of DW surface (Appendix A). We estimate σ_{ex} from the classical DW profile, $\sigma_{ex} = \int_{-\infty}^{+\infty} U_{12}(x)dx = \int_{-\infty}^{+\infty} -J_{AF}\mathbf{m}_1(x) \cdot \mathbf{m}_2(x)dx$, which yields

$$\sigma_{ex} = -2J_{AF}\Delta \frac{\delta q/\Delta}{\sinh \frac{\delta q}{\Delta}} \left(\cosh \frac{\delta q}{\Delta} - \cos(\delta \varphi) \right) + \text{const}$$

$$\approx -J_{AF}\Delta(\delta \varphi^2 + (\delta q/\Delta)^2) + \text{const}, \quad (9)$$

where the approximation is valid for small $\delta q/\Delta$ and $\delta \varphi$. Figure 6(b) shows the inter-exchange coupling surface energy versus δq and $\delta \varphi$. For δq larger than Δ, the dependence on $\delta \varphi$ disappears, but for small δq and $\delta \varphi$ the energy is nearly parabolic and given by the approximation above. This expression, by assuming a rigid DW profile, overestimates the coupling energy and can be expected to slightly underestimate δq and $\delta \varphi$.

This collective coordinates model covers a very large number of cases that are not always analytically solvable. We consider here the steady-state motion of the DW in translational or asymptotic precessional regimes. By assuming the bounded state of the two DWs, $\langle \delta \varphi \rangle \approx 0$ and $\langle \dot{\delta q} \rangle \approx 0$.

TABLE III. Collective coordinates model $(q, \varphi, \delta q, \delta \varphi)$ solutions for a DW driven by field, STT, or SOT in the studied CoGd (left column) and SAF cases (right column). In the CoGd, $D_2 = 0$, and current-induced torques only in the TM sublattice "1" $(\theta_{SHE2} = P_2 = \beta_2 = 0)$. In the SAF, the two layers have the same material parameters except $D_2 = 0$, and with current-induced torques only in the sublattice "1" $(\theta_{SHE2} = P_2 = \beta_2 = 0)$. In both cases, DMI is considered dominant relative to the dipolar-induced anisotropy $(K_{BN} = 0)$. δq and $\delta \varphi$ are considered constant in time. v_{eff}, φ_{eff} are the solutions of the q-φ model with effective parameters (Table I). The material parameters with no indices are the effective parameters defined in Sec. II.

	CoGd	SAF
Field-driven, Translational	$v = v_{eff}, \varphi = \varphi_{eff}$ $\delta q = -\Delta \mu_0 H \frac{L_{\alpha 1} M_2 + L_{\alpha 2} M_1}{L_\alpha}/J_{AF}$ $\delta \varphi = -v L_2/(\Delta J_{AF})$	$v = v_{eff}, \varphi = \varphi_{eff}$ $\delta q = -\Delta \mu_0 H M_1 \frac{2 t_1 t_2}{t}/J_{RKKY}$ $\delta \varphi = -v L_1 t_2/(\Delta J_{RKKY})$
Field-driven, Asympt. Precessional	$v = v_{eff}, \dot\varphi = \dot\varphi_{eff}$ $\delta q = -\Delta \mu_0 H \frac{L_S(L_1 M_2 - L_2 M_1) + L_\alpha(L_{\alpha 1} M_2 + L_{\alpha 2} M_1)}{L_S^2 + L_\alpha^2}/J_{AF}$ $\delta \varphi = -v \frac{L_1 L_2 (\alpha_1 + \alpha_2)}{L_\alpha}/(\Delta J_{AF})$	$v = v_{eff}, \dot\varphi = \dot\varphi_{eff}$ $\delta q = -\Delta \mu_0 H M_1 \frac{L_\alpha^2}{L_S^2 + L_\alpha^2} \frac{2 t_1 t_2}{t}/J_{RKKY}$ $\delta \varphi = -\mu_0 H M_1 \frac{L_S L_\alpha}{L_S^2 + L_\alpha^2} \frac{2 t_1 t_2}{t}/J_{RKKY}$
STT-driven, Translational	$v = v_{eff}, \varphi = \varphi_{eff}$ $\delta q = -v L_{\alpha 2}/J_{AF}$ $\delta \varphi = -v L_2/(\Delta J_{AF})$	$v = v_{eff}, \varphi = \varphi_{eff}$ $\delta q = 0$ $\delta \varphi = (v - u_1) L_{\alpha 1} t_2/J_{RKKY}$
STT-driven, Asympt. Precessional	$v = v_{eff}, \dot\varphi = \dot\varphi_{eff}$ $\delta q = -v L_2 \frac{\beta L_2 \alpha_2^2 - \beta L_S + L_1(\beta \alpha_1 \alpha_2 + \alpha_1 + \alpha_2)}{\beta L_\alpha + L_S}/J_{AF}$ $\delta \varphi = -v L_2 \frac{L_S - \alpha_2 L_\alpha + \beta L_1(\alpha_1 + \alpha_2)}{\beta L_\alpha + L_S}/(\Delta J_{AF})$	$v = v_{eff}, \dot\varphi = \dot\varphi_{eff}$ $\delta q = L_S u_1(\beta_1 - \alpha_1) \frac{L_1^2}{L_S^2 + L_\alpha^2} \frac{2 t_1 t_2}{t}/J_{RKKY}$ $\delta \varphi = L_{\alpha 1} u_1(\alpha_1 - \beta_1) \frac{L_1^2}{L_S^2 + L_\alpha^2} \frac{2 t_1 t_2}{t}/(\Delta J_{RKKY})$
SOT-driven	$v = v_{eff}, \varphi = \varphi_{eff}$ $\delta q = -v L_{\alpha 2}/J_{AF}$ $\delta \varphi = -v L_2/(\Delta J_{AF})$	$v = v_{eff}, \varphi = \varphi_{eff}$ $\delta q = \pm v L_{\alpha 1} t_2/J_{RKKY}$ $\delta \varphi = \pm v L_1 t_2/(\Delta J_{RKKY})$

This allows us to obtain analytically expressions for v, φ, $\delta \varphi$, and δq for all driving forces (field, STT, or SOT) in the two considered example systems, the CoGd film and the SAF, shown in Table III. In these solutions, we apply the previously discussed assumptions for CoGd ($t_1 = t_2 = t$, $P_2 = \beta_2 = \theta_{SHE2} = 0$, $D_2 = 0$), and for the SAF ($t = t_1 + t_2$, $\theta_{SHE2} = 0$, $D_2 = 0$, same values in layers "1" and "2" for the other parameters), and we have neglected the dipolar-induced planar anisotropy K_{BN}.

Interestingly, we found that this model gives the same steady-state results (v, φ, and $\dot\varphi$) as the simpler q-φ model with effective parameters for all driving forces (see Table III). This shows that the q-φ model, that was obtained in the strong-coupling approximation of perfect antiparallel alignment, is valid even for finite coupling. Furthermore, it shows that the DW dynamics are independent of J_{AF}.

B. Micromagnetic simulations

To verify this finding, we have repeated the micromagnetic simulations of a field-driven DW in CoGd with different values of the coupling constant J_{AF}, from $100\times$ to $0.01\times$ the previously used value (in Table II). For values of J_{AF} smaller than $0.01 \times J_{AF}$, the DWs decoupled. Figures 7(a) and 7(b) show the velocity v and precession rate $\dot\varphi$ versus H obtained with the various values of J_{AF} for %Co = 80% ($m_S = 0.07$). The color of the points indicates the value of J_{AF}. For the largest couplings ($100\times$ to $0.1\times$), v and $\dot\varphi$ coincide and are independent of J_{AF}, as predicted by the model. Significant deviations occur only for the lowest couplings at the highest

fields, where the DW structure is highly distorted. Similar results were obtained for the other driving forces (not shown).

The model predicts that the internal distortions, δq and $\delta \varphi$, are proportional to the ratio of the driving force and the interexchange coupling (e.g., H/J_{AF} for the field-driven DW), and so tend to zero for low driving forces or large coupling. Figures 7(c) and 7(d) show $\delta q/\Delta$ and $\delta \varphi$ versus H/J_{AF} for different J_{AF} (for %Co = 80%). Although δq is sometimes neglected (e.g., [44]), the magnitudes of $\delta \varphi$ and $\delta q/\Delta$ are comparable, and therefore produce comparable contributions to the system energy [Eq. (9)].

These distortions do not affect the DW velocity nor its precession, except at very low J_{AF}. The velocity with $100 \times J_{AF}$ and with $0.1\times$ is the same, even if δq and $\delta \varphi$ change by four orders of magnitude. Nevertheless, these distortions may be significant in the transient response [48]. The linear relation of δq and $\delta \varphi$ with H/J_{AF} predicted by the collective coordinates model can be clearly seen. As expected, the proportionality factors ($\frac{\delta q}{\Delta}/\frac{\mu_0 H}{J_{AF}}$ and $\frac{\delta \varphi}{\pi}/\frac{\mu_0 H}{J_{AF}}$) are different for the translational and precessional regimes. The proportionality factors also vary with l_S [shown in Figs. 8(a1) and 8(b1)] as predicted by the model (Table III). The same observation holds also for the SAF [shown in Figs. 8(a2) and 8(b2)].

In previous studies (e.g., [4,49]), the DW velocity was described as a function of the "exchange coupling torque" proportional to $J_{AF} \cos(\delta \varphi)$. However, the presented results show that the exchange coupling torque is not a convenient parameter, as the DW velocity does not directly depend on $\delta \varphi$ nor on the coupling torque. The coupling torque, being symmetric on the two sublattices, applies no net force on the
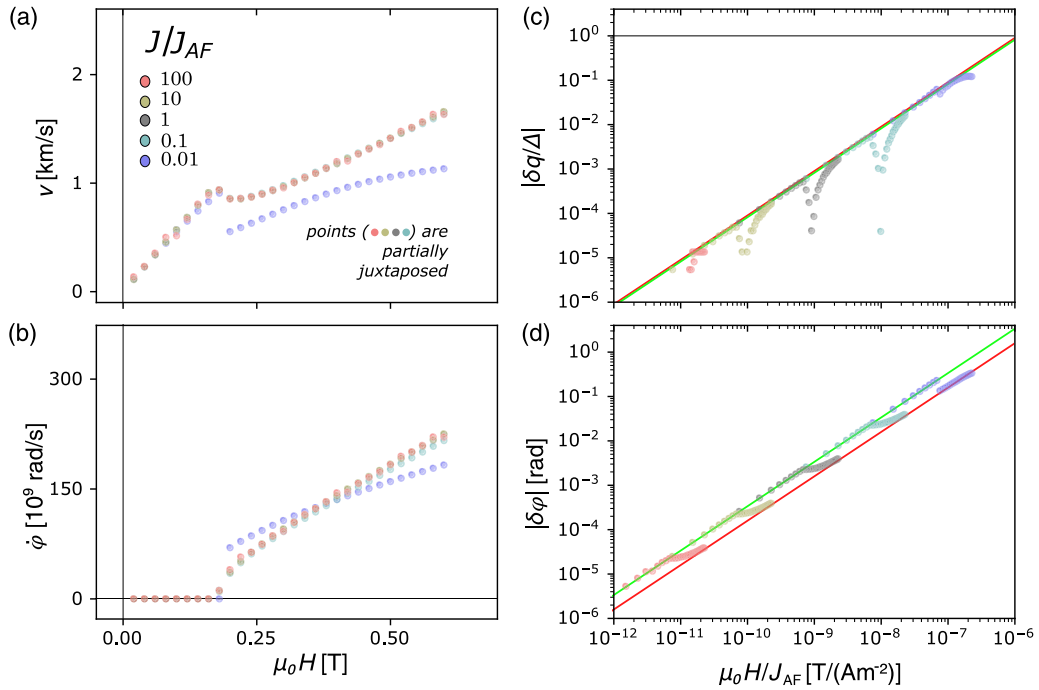
FIG. 7. Effect of intersublattice angle on the velocity and precession rate of a field-driven DW in CoGd (%Co = 80%, $m_S = 0.07$, $l_S = 0.018$). (a),(b) Comparison between the (a) velocity and (b) precession rate vs the applied field obtained with different values of coupling (ranging from $J/J_{AF} = 100$ to 0.01). Many points are juxtaposed. (c) $\delta q/\Delta$ and (d) $\delta\varphi$ vs the ratio H/J_{AF} for the same simulations as in (a). The lines correspond to the linear relations predicted by the model (Table III) for the translational (green) and asymptotic precessional (red) regimes.

DW, and may only influence the DW dynamics by distorting its structure.

These results validate the use of the q-φ model with effective parameters to interpret DW dynamics, even at moderate coupling strength, and the use of the collective coordinates

model to estimate the distortions of the DW pair (δq and $\delta\varphi$). Gomonay *et al.* [30] showed that the antiferromagnets can be described by a single effective equation describing the Néel vector field, with the antialignment distortion as a subordinate expression. Here, as well, the dynamics of q and φ do not
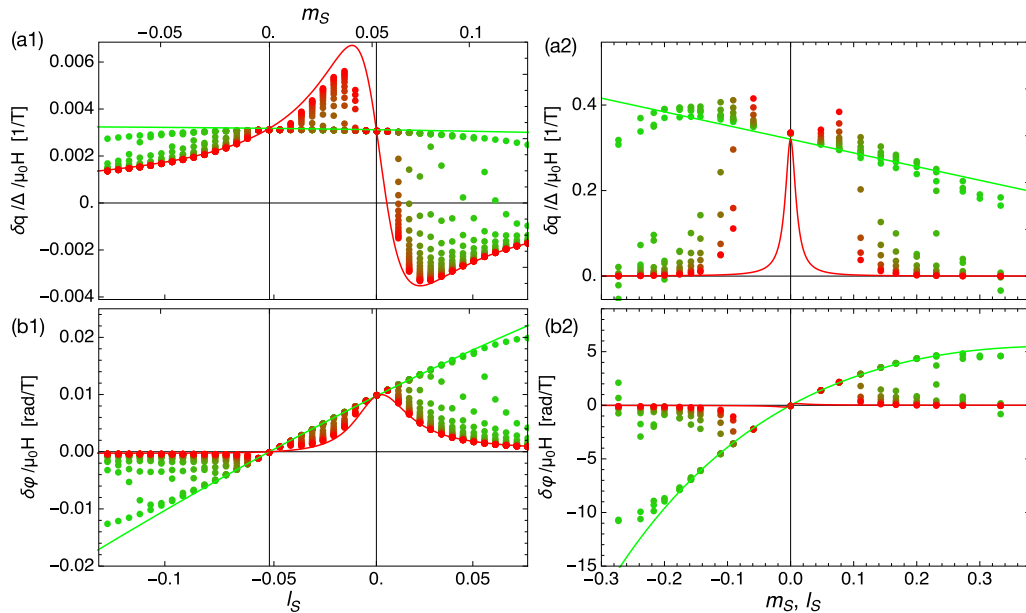

FIG. 8. Variation of interlattice distortions, δq and $\delta\varphi$, with m_S of a field-driven DW in CoGd (a1),(b1) and in the SAF (a2),(b2). (a1),(a2) $\delta q/(H/J_{AF})$ and (b1),(b2) $\delta\varphi/(H/J_{AF})$ vs l_S. The lines are the analytical laws given by the collective coordinates model for the translational (green) and precessional (red) regimes (Table III). The color code of the points is the same as in Fig. 3.

depend on δq and $\delta\varphi$. The current result, although stricter in application domain (1D DW dynamics instead of the general LLG), suggests that such a description may be true in the wider class of ferrimagnetic systems.

V. CONCLUSION

Using analytical and numerical methods, we have studied the dynamics of magnetic DWs in systems with two antiferromagnetically coupled sublattices, in particular in ferrimagnets and SAFs, under different driving forces: magnetic field, STT, and interfacial SOT. By comparing it to micromagnetic simulations, we have shown that the q-φ model using effective parameters provides a unified, analytical description of DW dynamics in multilattice systems. Moreover, we have shown that this description is valid even far from the strong-coupling limit, where the sublattices are not perfectly antiparallel. The same approach, using effective parameters, could be applied to other systems (e.g., multilayered systems) or other magnetic textures (e.g., vortices or skyrmions).

In tunable systems, where the ratio of the sublattice moments can be changed, the models predict that the DW dynamics can differ significantly from the ferromagnetic case in the vicinity of the compensation points (ACP and MCP). Depending on the driving force, the DW may show features with great interest for applications, such as enhanced mobility or suppression of precession. As we have discussed, some of these features can be seen in recently reported results on DW dynamics in systems like ferrimagnets or synthetic antiferromagnets, while other predicted features are yet to be observed.

ACKNOWLEDGMENTS

APPENDIX A: THE q-φ MODEL

The q-φ model is deduced from the LLG equation by assuming a Bloch DW profile, where the magnetization in spherical coordinates, $(\Theta(x), \phi(x))$, follows,

$$\phi(x) = \varphi, \quad \Theta(x) = 2\arctan\left(\exp(x-q)/\Delta\right),$$

where φ is the in-plane angle of the magnetization of the DW (independent of x), q is the position of the DW center, and Δ is the Bloch DW width parameter [see Fig. 1(c)]. The DW dynamics under driving forces (field **H** or electrical current J) can be described via the time evolution of the two coupled collective coordinates (q and φ):

$$\alpha\frac{\dot{q}}{\Delta} + \dot{\varphi} = \gamma_0 H_z - \frac{\partial_q \sigma_{ex}}{2L_S} + \frac{\pi}{2}\frac{\tau_{DL}}{L_S}\cos\varphi + \beta\frac{u}{\Delta},$$

$$\frac{\dot{q}}{\Delta} - \alpha\dot{\varphi} = \gamma_0 H_{BN}\frac{\sin(2\varphi)}{2} + \frac{\pi}{2}\gamma_0(H_{DMI} + H_x)\sin\varphi$$
$$- \left(\gamma_0 H_y + \frac{\tau_{FL}}{L_S}\right)\cos\varphi + \frac{\partial_\varphi \sigma_{ex}}{2\Delta L_S} + \frac{u}{\Delta}. \quad \text{(A1)}$$

The term σ_{ex} accounts for the other energy terms of the system (such as the interlattice exchange coupling in Sec. IV), $H_{DMI} = \frac{D/\Delta}{\mu_0 M_S}$ accounts for the DMI, and $H_{BN} = \frac{2K_{BN}}{\mu_0 M_S}$ accounts for the in-plane (Bloch/Néel) dipolar-induced anisotropy. For thin films with spatially merged sublattices, $K_{BN} \approx \frac{\ln 2}{2\pi}\frac{t}{\Delta}\mu_0 M_S^2$ [50]. For systems with spatially separated sublattices, the same approximation would yield $K_{BN} \approx \frac{\ln 2}{2\pi}\mu_0(t_1^2 M_1^2 + t_2^2 M_2^2)/(t\Delta)$, but the dipolar interactions between the DWs in the two layers will decrease it by orders of magnitude [5] and so K_{BN} may be neglected in the presence of DMI. In agreement with this description, two steady-state DW propagation regimes can exist [36]: the translational regime at low drive, with a constant velocity and fixed DW angle ($\dot{\varphi} = 0$), and the precessional regime at high drive, with oscillating velocity and oscillating DW angle. The two regimes are separated by the Walker threshold [36–39], which is the

TABLE IV. q-φ model solutions [Eq. (A1)] for v, φ, $\dot{\varphi}$, and the Walker threshold of a DW in a ferromagnet with perpendicular anisotropy driven by field, STT, or SOT in translational and asymptotic precessional regimes [36–38]. The top and bottom expressions for φ and Walker thresholds refer to the case of dominant dipolar-induced Bloch-Néel anisotropy (K_{BN}) or dominant DMI (D). Here, $H_x = H_y = H_{FL} = 0$. $H_{BN} = \frac{2K_{BN}}{\mu_0 M_S}$, $H_{DMI} = \frac{D/\Delta}{\mu_0 M_S}$.

Field-driven

	Translational regime	Walker threshold	Asympt. Precessional regime	
$v = \frac{\Delta}{\alpha}\gamma_0 H$	$\varphi = \begin{cases} \frac{1}{2}\arcsin(H/H_W) \\ \arcsin(H/H_W) \end{cases}$	$\|H_W\| = \begin{cases} \frac{1}{2}\|\alpha H_{BN}\| \\ \frac{\pi}{2}\|\alpha H_{DMI}\| \end{cases}$	$v = \frac{\Delta\alpha}{1+\alpha^2}\gamma_0 H$	$\dot{\varphi} = \frac{1}{1+\alpha^2}\gamma_0 H$

STT-driven

	Translational regime	Walker threshold	Asympt. Precessional regime	
$v = \frac{\beta}{\alpha}u$	$\varphi = \begin{cases} \frac{1}{2}\arcsin(u/u_W) \\ \arcsin(u/u_W) \end{cases}$	$\|u_W\| = \begin{cases} \frac{1}{2}\left\|\frac{\alpha\Delta\gamma_0 H_{BN}}{\beta-\alpha}\right\| \\ \frac{\pi}{2}\left\|\frac{\alpha\Delta\gamma_0 H_{DMI}}{\beta-\alpha}\right\| \end{cases}$	$v = \frac{1+\alpha\beta}{1+\alpha^2}u$	$\dot{\varphi} = \frac{\beta-\alpha}{1+\alpha^2}\frac{u}{\Delta}$

SOT-driven

$v = \frac{\Delta}{\alpha}\frac{\pi}{2}\frac{\tau_{SHE}}{L_S}\cos\varphi$	$\varphi = \arctan\left(\frac{\tau_{SHE}}{\alpha M_S \mu_0 H_{DMI}}\right)$			

TABLE V. List of symbols used in the text. Parameters with indices 1 and 2 refer to the sublattice parameters.

Symbol	Units	Usage	Description
$\mathbf{m}$, $\mathbf{M}$	–, A/m	Eqs. (1),(2)	Normalized magnetization and magnetization, $\mathbf{M} = M_S\mathbf{m}$
M_S, M_1, M_2	A/m	Eq. (5)	Spontaneous magnetization
L_S, L_1, L_2	Kg/(ms)	Eqs. (2),(5)	Angular momentum density
m_S		Eq. (8)	Normalized magnetization
l_S		Eq. (8)	Normalized angular momentum
γ, γ_0	s^{-1}/T, s^{-1}/(A/m)	Eq. (1)	Gyromagnetic ratio. $\gamma_0 = \mu_0\gamma = \mu_0 M_S/L_S$
g			Landé g-factor, $\gamma = g\mu_B/\hbar$, where μ_B is the Bohr magneton
α		Eqs. (1),(5)	Gilbert damping parameter, $\alpha = L_\alpha/L_S$
$L_\alpha, L_{\alpha 1}, L_{\alpha 2}$	sJ/m^3	Eqs. (2),(5)	Product αL_S
t, t_1, t_2	m		Film (sublattice) thickness
$\mathcal{H}$	A/m		Effective field, $\mathcal{H} \equiv \frac{-1}{\mu_0 M_S}\delta_\mathbf{m} U$
$\delta_\mathbf{m} U$	J/m^3	Eq. (2)	Variational derivative of $U(\mathbf{m}(\mathbf{r}))$
U, U_1, U_2	J/m^3	Appendix B	Total energy (density), $U = U_{\text{Zeeman}} + U_K + U_{\text{ex}} + U_{\text{DMI}} + U_{\text{demag}}$ (due to Zeeman, anisotropy, exchange, Dzyaloshinskii-Moriya, and dipolar effects)
σ_{ex}	J/m^2	Appendix A	Interlattice coupling energy per DW surface
$K, K_1, K_2, K_{\text{dipolar}}$	J/m^3	Appendix B	Effective, internal and dipolar-induced uniaxial anisotropy.
K_{BN}	J/m^3	Appendix A	Dipolar-induced in-plane (Bloch/Néel) DW anisotropy
A, A_1, A_2	J/m	Appendix B	Exchange stiffness
D, D_1, D_2	J/m^2	Appendix B	DMI parameter
J_{AF}	J/m^3	Appendix B	Coupling between sublattices (volumic energy density)
J_{RKKY}	J/m^2	Appendix B	Coupling between the two layers of the SAF (areal energy density), $J_{\text{AF}} = J_{\text{RKKY}}/t$
$\boldsymbol{\tau}, \boldsymbol{\tau}_{\text{STT}}, \boldsymbol{\tau}_{\text{SOT}}, \boldsymbol{\tau}_{\text{FL}}, \boldsymbol{\tau}_{\text{DL}}$	Nm/m^3	Eq. (2)	Nonconservative torques, which include the STT, SOT, field-like SOT, and damping-like SOT
τ_{SHE}	Nm/m^3		SHE-induced SOT, $\tau_{\text{SHE}} = J\theta_{\text{SHE}}\hbar/(2et)$
$\mathbf{u}$	m/s		STT parameter, $L_S\mathbf{u} = PJ\hbar/(2e)\mathbf{e}_J$
β, β_1, β_2		Eq. (7)	STT nonadiabatic parameter
P, P_1, P_2		Eq. (7)	Current spin polarization (STT)
$\theta_{\text{SHE}}, \theta_{\text{SHE1}}, \theta_{\text{SHE2}}$		Eq. (7)	SHE angle
v	m/s		DW velocity
q	m	Appendix A	DW position (q-φ model)
φ	(rad)	Appendix A	In-plane angle of DW magnetization (q-φ model)
Δ	m	Appendix A	Bloch DW width parameter
δq	m	Section IV	DW position difference
$\delta\varphi$	(rad)	Section IV	DW in-plane angle difference
H_W	A/m		Walker threshold (field-driven)
J_W	A/m^2		Walker threshold (STT-driven)

maximum driving force that still satisfies the condition $\dot{\varphi} = 0$. In the limit of high drive, the DW approaches the asymptotic precessional regime, where $\dot{\varphi} \gg 0$, and it is possible to consider that $\langle\sin\varphi\rangle \approx \langle\cos\varphi\rangle \approx 0$. Note that for a DW driven by SHE alone, the precessional regime does not exist [38]. The velocity $v = \dot{q}$, the internal angle φ, and the precession rate $\dot{\varphi}$ for a DW driven by field, SOT, or STT in the translational and the asymptotic precessional regimes, deduced from Eq. (A1), are shown in Table IV. This model can also be applied to DWs in in-plane magnetized systems, with the due adaptations of the effective fields.

APPENDIX B: MICROMAGNETIC ENERGY TERMS

The usual energy volumic density terms due to Zeeman energy, uniaxial anisotropy, exchange stiffness, DMI, and de-magnetizing field ($\mathbf{H}_{\text{demag}}$) are

$$U_{\text{Zeeman}} = -\mu_0 M_S \mathbf{m} \cdot \mathbf{H}_0, \quad U_K = -K(\mathbf{m} \cdot \mathbf{z})^2,$$

$$U_{\text{ex}} = A|\nabla\mathbf{m}|^2, \quad U_{\text{DMI}} = D[m_z\nabla \cdot \mathbf{m} - (\mathbf{m} \cdot \nabla)m_z],$$

$$U_{\text{demag}} = -\tfrac{1}{2}\mu_0 M_S \mathbf{m} \cdot \mathbf{H}_{\text{demag}}.$$

In double lattice systems, the intersublattice exchange coupling can be expressed as $U_{12} = -J_{\text{AF}}\mathbf{m}_1 \cdot \mathbf{m}_2$. In the SAF, the RKKY coupling is an interface effect. As we only consider the limit of thin films in this article (i.e., $\partial_z\mathbf{m} \approx 0$), the same form of U_{12} can be used, with J_{RKKY}/t replacing J_{AF}, J_{RKKY} being an areal energy density.

Note again that for the reader's convenience, all used symbols and their definitions are listed in Table V.

[1] A. Manchon, J. Železný, I. M. Miron, T. Jungwirth, J. Sinova, A. Thiaville, K. Garello, and P. Gambardella, Current-induced spin-orbit torques in ferromagnetic and antiferromagnetic systems, Rev. Mod. Phys. **91**, 035004 (2019).

[2] C. O. Avci, E. Rosenberg, L. Caretta, F. Büttner, M. Mann, C. Marcus, D. Bono, C. A. Ross, and G. S. D. Beach, Interface-driven chiral magnetism and current-driven domain walls in insulating magnetic garnets, Nat. Nanotechnol. **14**, 561 (2019).

[3] T. Jungwirth, X. Marti, P. Wadley, and J. Wunderlich, Antiferromagnetic spintronics, Nat. Nanotechnol. **11**, 231 (2016).

[4] S.-H. Yang, K.-S. Ryu, and S. Parkin, Domain-wall velocities of up to 750 m s^{-1} driven by exchange-coupling torque in synthetic antiferromagnets, Nat. Nanotechnol. **10**, 221 (2015).

[5] A. Hrabec, V. Križáková, S. Pizzini, J. Sampaio, A. Thiaville, S. Rohart, and J. Vogel, Velocity Enhancement by Synchronization of Magnetic Domain Walls, Phys. Rev. Lett. **120**, 227204 (2018).

[6] A. Hrabec, J. Sampaio, M. Belmeguenai, I. Gross, R. Weil, S. M. Chérif, A. Stashkevich, V. Jacques, A. Thiaville, and S. Rohart, Current-induced skyrmion generation and dynamics in symmetric bilayers, Nat. Commun. **8**, 15765 (2017).

[7] K.-J. Kim, S. K. Kim, Y. Hirata, S.-H. Oh, T. Tono, D.-H. Kim, T. Okuno, W. S. Ham, S. Kim, G. Go, Y. Tserkovnyak, A. Tsukamoto, T. Moriyama, K.-J. Lee, and T. Ono, Fast domain wall motion in the vicinity of the angular momentum compensation temperature of ferrimagnets, Nat. Mater. **16**, 1187 (2017).

[8] S. A. Siddiqui, J. Han, J. T. Finley, C. A. Ross, and L. Liu, Current-Induced Domain Wall Motion in a Compensated Ferrimagnet, Phys. Rev. Lett. **121**, 057701 (2018).

[9] L. Caretta, M. Mann, F. Büttner, K. Ueda, B. Pfau, C. M. Günther, P. Hessing, A. Churikova, C. Klose, M. Schneider, D. Engel, C. Marcus, D. Bono, K. Bagschik, S. Eisebitt, and G. S. D. Beach, Fast current-driven domain walls and small skyrmions in a compensated ferrimagnet, Nat. Nanotechnol. **13**, 1154 (2018).

[10] Y. Hirata, D.-H. Kim, S. K. Kim, D.-K. Lee, S.-H. Oh, D.-Y. Kim, T. Nishimura, T. Okuno, Y. Futakawa, H. Yoshikawa, A. Tsukamoto, Y. Tserkovnyak, Y. Shiota, T. Moriyama, S.-B. Choe, K.-J. Lee, and T. Ono, Vanishing skyrmion Hall effect at the angular momentum compensation temperature of a ferrimagnet, Nat. Nanotechnol. **14**, 232 (2019).

[11] S. Woo, K. M. Song, X. Zhang, Y. Zhou, M. Ezawa, X. Liu, S. Finizio, J. Raabe, N. J. Lee, S.-I. Kim, S.-Y. Park, Y. Kim, J.-Y. Kim, D. Lee, O. Lee, J. W. Choi, B.-C. Min, H. C. Koo, and J. Chang, Current-driven dynamics and inhibition of the skyrmion Hall effect of ferrimagnetic skyrmions in GdFeCo films, Nat. Commun. **9**, 959 (2018).

[12] E. Haltz, J. Sampaio, R. Weil, Y. Dumont, and A. Mougin, Strong current actions on ferrimagnetic domain walls in the creep regime, Phys. Rev. B **99**, 104413 (2019).

[13] E. Haltz, J. Sampaio, S. Krishnia, L. Berges, R. Weil, and A. Mougin, Measurement of the tilt of a moving domain wall shows precession-free dynamics in compensated ferrimagnets, Sci. Rep. **10**, 16292 (2020).

[14] T. Shiino, S.-H. Oh, P. M. Haney, S.-W. Lee, G. Go, B.-G. Park, and K.-J. Lee, Antiferromagnetic Domain Wall Motion Driven by Spin-Orbit Torques, Phys. Rev. Lett. **117**, 087203 (2016).

[15] F. Keffer and C. Kittel, Theory of antiferromagnetic resonance, Phys. Rev. **85**, 329 (1952).

[16] P. Stremoukhov, A. Safin, M. Logunov, S. Nikitov, and A. Kirilyuk, Spintronic terahertz-frequency nonlinear emitter based on the canted antiferromagnet-platinum bilayers, J. Appl. Phys. **125**, 223903 (2019).

[17] S.-H. Oh, S. K. Kim, D.-K. Lee, G. Go, K.-J. Kim, T. Ono, Y. Tserkovnyak, and K.-J. Lee, Coherent terahertz spin-wave emission associated with ferrimagnetic domain wall dynamics, Phys. Rev. B **96**, 100407(R) (2017).

[18] S. Lepadatu, H. Saarikoski, R. Beacham, M. J. Benitez, T. A. Moore, G. Burnell, S. Sugimoto, D. Yesudas, M. C. Wheeler, J. Miguel, S. S. Dhesi, D. McGrouther, S. McVitie, G. Tatara, and C. H. Marrows, Synthetic ferrimagnet nanowires with very low critical current density for coupled domain wall motion, Sci. Rep. **7**, 1640 (2017).

[19] R. A. Duine, K.-J. Lee, S. S. P. Parkin, and M. D. Stiles, Synthetic antiferromagnetic spintronics, Nat. Phys. **14**, 217 (2018).

[20] S. S. P. Parkin, N. More, and K. P. Roche, Oscillations in Exchange Coupling and Magnetoresistance in Metallic Superlattice Structures: Co/Ru, Co/Cr, and Fe/Cr, Phys. Rev. Lett. **64**, 2304 (1990).

[21] S. S. P. Parkin, Systematic Variation of the Strength and Oscillation Period of Indirect Magnetic Exchange Coupling Through the 3d, 4d, and 5d Transition Metals, Phys. Rev. Lett. **67**, 3598 (1991).

[22] P. Hansen, C. Clausen, G. Much, M. Rosenkranz, and K. Witter, Magnetic and magneto-optical properties of rare-earth transition-metal alloys containing Gd, Tb, Fe, Co, J. Appl. Phys. **66**, 756 (1989).

[23] Y. Hirata, D.-H. Kim, T. Okuno, T. Nishimura, D.-Y. Kim, Y. Futakawa, H. Yoshikawa, A. Tsukamoto, K.-J. Kim, S.-B. Choe, and T. Ono, Correlation Between Compensation Temperatures of Magnetization and Angular Momentum in GdFeCo Ferrimagnets, Phys. Rev. B **97**, 220403(R) (2018).

[24] F. B. Hagedorn, Domain wall motion in bubble domain materials, AIP Conf. Proc. **5**, 72 (1972).

[25] L. D. Landau and E. Lifshitz, On the theory of the dispersion of magnetic permeability in ferromagnetic bodies, Phys. Z. Sowjet. **8**, 153 (1935).

[26] T. Gilbert, A phenomenological theory of damping in ferromagnetic materials, IEEE Trans. Magn. **40**, 3443 (2004).

[27] G. P. Vella-Coleiro, Domain wall mobility in epitaxial garnet films, AIP Conf. Proc. **10**, 424 (1973).

[28] If $\boldsymbol{\tau} \neq 0$, the energy variation is instead $d_t U = -L_\alpha |\partial_t \mathbf{m}|^2 + \frac{1}{L_S} \boldsymbol{\tau} \cdot (L_\alpha \partial_t \mathbf{m} + \delta_\mathbf{m} U)$, or $d_t U = -\frac{L_\alpha}{L_S^2 + L_\alpha^2} (|\mathbf{m} \times \delta_\mathbf{m} U|^2 - \boldsymbol{\tau} \cdot (\mathbf{m} \times \delta_\mathbf{m} U)) + \frac{L_S}{L_S^2 + L_\alpha^2} \delta_\mathbf{m} U \cdot \boldsymbol{\tau}$.

[29] A. Thiaville, Y. Nakatani, J. Miltat, and Y. Suzuki, Micromagnetic understanding of current-driven domain wall motion in patterned nanowires, Europhys. Lett. **69**, 990 (2005).

[30] E. V. Gomonay and V. M. Loktev, Spintronics of antiferromagnetic systems (Review Article), Low Temp. Phys. **40**, 17 (2014).

[31] R. K. Wangsness, Sublattice effects in magnetic resonance, Phys. Rev. **91**, 1085 (1953).

[32] R. Bläsing, T. Ma, S.-H. Yang, C. Garg, F. K. Dejene, A. T. N'Diaye, G. Chen, K. Liu, and S. S. P. Parkin, Exchange coupling torque in ferrimagnetic Co/Gd bilayer maximized near

angular momentum compensation temperature, Nat. Commun. **9**, 4984 (2018).

[33] D.-H. Kim, T. Okuno, S. K. Kim, S.-H. Oh, T. Nishimura, Y. Hirata, Y. Futakawa, H. Yoshikawa, A. Tsukamoto, Y. Tserkovnyak, Y. Shiota, T. Moriyama, K.-J. Kim, K.-J. Lee, and T. Ono, Low Magnetic Damping of Ferrimagnetic GdFeCo Alloys, Phys. Rev. Lett. **122**, 127203 (2019).

[34] I. Ng, S. K. Kim, and Q. Shao, Survey of temperature dependence of the damping parameter in the ferrimagnet $Gd_3Fe_5O_{12}$, arXiv:2009.12073 [cond-mat.mtrl-sci].

[35] S. Krishnia, E. Haltz, L. Berges, L. Aballe, M. Foerster, L. Bocher, R. Weil, A. Thiaville, J. Sampaio, and A. Mougin, Making spin-orbit coupling visible in single layer ferrimagnets: Direct observation of spin-orbit torques and chiral spin textures, arXiv:2007.07569.

[36] N. L. Schryer and L. R. Walker, The motion of 180 domain walls in uniform dc magnetic fields, J. Appl. Phys. **45**, 5406 (1974).

[37] A. Mougin, M. Cormier, J. Adam, P. J. Metaxas, and J. Ferré, Domain wall mobility, stability and Walker breakdown in magnetic nanowires, Europhys. Lett. **78**, 57007 (2007).

[38] A. Thiaville, S. Rohart, E. Jué, V. Cros, and A. Fert, Dynamics of Dzyaloshinskii domain walls in ultrathin magnetic films, Europhys. Lett. **100**, 57002 (2012).

[39] A. Malozemoff and J. Slonczewski, *Magnetic Domain Walls in Bubble Materials* (Academic, New York, 1979), pp. 269–292.

[40] A. Vansteenkiste, J. Leliaert, M. Dvornik, M. Helsen, F. Garcia-Sanchez, and B. Van Waeyenberge, The design and verification of MuMax3, AIP Adv. **4**, 107133 (2014).

[41] E. Haltz, R. Weil, J. Sampaio, A. Pointillon, O. Rousseau, K. March, N. Brun, Z. Li, E. Briand, C. Bachelet, Y. Dumont, and A. Mougin, Deviations from bulk behavior in TbFe(Co) thin films: Interfaces contribution in the biased composition, Phys. Rev. Mater. **2**, 104410 (2018).

[42] If P_1 and P_2 have the same sign, $v = 0$ occurs at $L_S = -\beta L_\alpha$. If the signs are opposite, it occurs at $\beta_1 P_1 t_1 + \beta_2 P_2 t_2 = 0$ since β_1 and β_2 are positive.

[43] T. Okuno, D.-H. Kim, S.-H. Oh, S. K. Kim, Y. Hirata, T. Nishimura, W. S. Ham, Y. Futakawa, H. Yoshikawa, A. Tsukamoto, Y. Tserkovnyak, Y. Shiota, T. Moriyama, K.-J. Kim, K.-J. Lee, and T. Ono, Spin-transfer torques for domain wall motion in antiferromagnetically coupled ferrimagnets, Nat. Electron. **2**, 389 (2019).

[44] E. Martinez, V. Raposo, and Ó. Alejos, Current-driven domain wall dynamics in ferrimagnets: Micromagnetic approach and collective coordinates model, J. Magn. Magn. Mater. **491**, 165545 (2019).

[45] R. J. Gambino and J. J. Cuomo, Selective resputtering-induced anisotropy in amorphous films, J. Vac. Sci. Technol. **15**, 296 (1978).

[46] B. Hebler, A. Hassdenteufel, P. Reinhardt, H. Karl, and M. Albrecht, Ferrimagnetic TbFe alloy thin films: Composition and thickness dependence of magnetic properties and all-optical switching, Front. Mater. **3**, 8 (2016).

[47] S. H. Yang, C. Garg, and S. S. Parkin, Chiral exchange drag and chirality oscillations in synthetic antiferromagnets, Nat. Phys. **15**, 543 (2019).

[48] J.-Y. Chauleau, R. Weil, A. Thiaville, and J. Miltat, Magnetic domain walls displacement: Automotion versus spin-transfer torque, Phys. Rev. B **82**, 214414 (2010).

[49] S. Krishnia, P. Sethi, W. L. Gan, F. N. Kholid, I. Purnama, M. Ramu, T. S. Herng, J. Ding, and W. S. Lew, Role of RKKY torque on domain wall motion in synthetic antiferromagnetic nanowires with opposite spin Hall angles, Sci. Rep. **7**, 11715 (2017).

[50] S. Tarasenko, A. Stankiewicz, V. Tarasenko, and J. Ferré, Bloch wall dynamics in ultrathin ferromagnetic films, J. Magn. Magn. Mater. **189**, 19 (1998).